A&A 382, 639–649 (2002)
DOI: 10.1051/0004-6361:20011645


Astronomy & Astrophysics

# Physical consequences of the inclusion of anomalous resistivity in the dynamics of 2D magnetic reconnection

I. Roussev[1,2], K. Galsgaard[3], and P. G. Judge[1]

[1] High Altitude Observatory, NCAR, 3450 Mitchell Lane, Boulder, CO 80301, USA
e-mail: judge@ucar.edu
[2] Armagh Observatory, College Hill, Armagh, BT61 9DG, N. Ireland
[3] University of St. Andrews, School of Mathematics and Statistics, North Haugh, St. Andrews, Fife, KY16 9SS, Scotland
e-mail: klaus@mcs.st-and.ac.uk

Received 14 August 2001 / Accepted 15 November 2001

**Abstract.** The aim of the present paper is to explore the role of anomalous resistivity on the dynamics of magnetic reconnection in a 2D environment of relevance to the solar transition region. We adopt an ad hoc but explicit form of the anomalous resistivity, motivated by a streaming instability, in which the resistivity jumps suddenly as the electron drift velocity exceeds some fraction of the mean electron thermal speed. Experiments have been conducted to investigate the impact of various critical speeds and arbitrary scaling constants of the resistivity level on the time-dependent evolution of the magnetic reconnection process. The specific threshold value is found to influence the dynamics of the reconnection, with higher values providing a localised on-off effect of patchy diffusion. For a given normalised value of the anomalous resistivity, the amount of Joule heating released scales inversely with the threshold value. The total energy release is found to be above the lower limit of "quiet" Sun nano-flares required to maintain a hot corona. The reconnection events discussed here may be important to the energy balance of the solar transition region and overlying corona, as already suggested in earlier work based on SUMER observations.

**Key words.** MHD – Sun: atmosphere – Sun: transition region – Sun: magnetic fields

## 1. Introduction

In the magnetohydrodynamic approximation, the coefficient of resistivity, $\eta$, represents Ohm's law, the ratio of the electric field strength to the current density locally in the rest frame moving with the fluid. This transport coefficient is usually derived from the kinetic theory of particle collisions in either a fully or partially ionised gas (the former case was presented by, e.g., Spitzer 1962). It is well known, however, that under some conditions of importance in astrophysical plasmas, the growth of plasma instabilities can radically affect the dynamics of the current-carrying charged particles, leading to plasma turbulence, with accompanying large changes in the effective resistivity (e.g., Parker 1994, Sect. 2.4.3). These effects, which serve to increase $\eta$, are known collectively as *anomalous resistivity*.

Owing to complexities of the plasma dynamics, anomalous resistivity is very poorly understood, and is often parameterised in ad hoc formalisms which have only hypothetical or semi-empirical support (see, e.g., de Kluiver et al. 1991; Somov et al. 2000). Nevertheless, anomalous resistivity is expected to be important for many reasons (e.g., Parker 1994). For example, this may initiate *fast magnetic reconnection*, i.e., reconnection that does not depend on the plasma resistivity (according to Lazarian & Vishniac 2000), with accompanying consequences for flares (e.g., Magara et al. 1996, 1997), CME's (e.g., Low 1994), and other observed solar phenomena. Spatial and temporal variations in $\eta$ may also produce changes in the field topology, and thus one can expect anomalous resistivity to further amplify such variations. For example, Parker (1994, Sect. 10.5) showed that a local maximum in anomalous resistivity produces mutual wrapping of magnetic flux bundles that are otherwise not entangled. This and other examples (e.g., Somov et al. 2000) show that the basic structure and evolution of space plasmas can be expected

*Send offprint requests to*: I. Roussev,
e-mail: ilr@ucar.edu

to depend critically on anomalous resistivity, if and when it is present.

The purpose of the present work is to examine influences that anomalous resistivity might have on a particular 2D MHD simulation studied in earlier work (Roussev et al. 2001). We will adopt an ad hoc description of this process with some justification. The particular situation describes the reconnection of magnetic fields in a vertically oriented current sheet whose thermal and magnetic structure represent conditions approximating the solar transition region. The reconnection process is initiated again in an ad hoc manner by enhancing the resistivity[1] locally and for a short period of time in the current sheet. The dynamic evolution of magnetic reconnection for a long duration of the "driving" process was reported in Roussev et al. (2001). Our task now is to investigate again the dynamics of this evolving system, but including the effects of anomalous resistivity with an explicit form different than that used to initiate the reconnection process. We will look specifically for changes in the morphology of magnetic fields, for evidence of small-scale flaring activity, and for evidence that the system is governed to some degree by a threshold criterion that might be characteristic of the sudden onset of anomalous resistivity. The latter is considered to be driven by streaming instabilities developed in a turbulent current sheet.

In Sect. 2.1 we discuss our adopted prescription and underlying physics for anomalous resistivity. The set of basic equations of magnetohydrodynamics (MHD) is given in Sect. 2.2, and the choice of initial configuration is made in Sect. 2.3. The driver of magnetic reconnection is presented in Sect. 2.4, and Sect. 2.5 describes the parameters space we investigate. In Sect. 3 we discuss the numerical results. Final conclusions are drawn in Sect. 4.

## 2. Physical description of the problem

### 2.1. Anomalous resistivity

We draw this brief physical summary largely from Parker (1994, Sect. 2.4.3). Electrical currents, carried mostly by the electrons, can lead to streaming instabilities, exciting a variety of modes of plasma oscillation which collectively lead to turbulence. The result is that the energy carried by the electrical current is efficiently converted to turbulent motions which, through Coulomb collisions, rapidly heat the electrons. These instabilities begin when the electron drift speed $v_{\rm dr}$, which is the electric current density $j$ divided by the charge density $e\,n_{\rm e}$, i.e., $v_{\rm dr} = j/(e\,n_{\rm e})$, exceeds certain critical values, depending on the particular mode. For example, the ion-acoustic mode is generated when $v_{\rm dr} > v_{\rm i}$, where $v_{\rm i}$ is the mean thermal ion speed. This is just the highest threshold mode of several which have smaller threshold values for onset, but these are all strongly suppressed by ion Landau damping, unless the electron temperature, $T_{\rm e}$, greatly exceeds the ion temperature, $T_{\rm i}$. In the present study, we will assume $T_{\rm e} \approx T_{\rm i}$ because of the efficient collisional coupling between the electron and ion fluids. We will return to this important issue again in Sect. 4.

When $T_{\rm e} \cong T_{\rm i}$, a different streaming instability will occur when $v_{\rm dr} \sim \xi$, where $\xi = \sqrt{k_{\rm B}\,T_{\rm e}/m_{\rm e}}$ is the mean thermal speed of electrons, leading to the excitation of electron plasma waves (Fried & Gould 1961). In essence, following a heuristic argument by Buneman (1958), we expect the effective collision time to be reduced from the kinetic value to the much smaller value $2\,\pi/\omega_{\rm pe}$, where $\omega_{\rm pe}$ is the electron plasma frequency, enhancing the resistivity accordingly.

The above physical picture leads us to parameterize the anomalous resistivity as

$$\hat{\eta}^* = \begin{cases} \eta_{\rm a}^* \left(\frac{|v_{\rm dr}|}{v_{\rm thr}} - 1\right); & |v_{\rm dr}| \geq v_{\rm thr}, \\ 0; & |v_{\rm dr}| < v_{\rm thr}. \end{cases} \quad (1)$$

Here $v_{\rm thr}$ is a threshold speed (of the order of the mean thermal speed of electrons) and $\eta_{\rm a}^*$ is a normalized value of this new resistivity. In physical units, the anomalous resistivity, $\hat{\eta}$, is given through $\hat{\eta} = \hat{\eta}^*\,V_{A0}\,L_0$. Here $V_{A0}$ and $L_0$ are the normalization units of velocity and length scale, respectively. Other choices are of course possible, including semi-empirical results based upon laboratory measurements (de Kluiver et al. 1991), and have been adopted by other authors (see the discussion by Somov et al. 2000). In essence though, all these parameterizations differ only in details but share the common physical basis of a streaming instability triggered by drift velocity or currents that exceed critical values.

From a numerical perspective, there are studies (e.g., Nishikawa & Neubert 1996; Silberstein & Otani 1994) aimed at exploring the nature of anomalous resistivity using particle codes, but these are not able to handle the proper ratio of electron to ion mass in a finite computing time. This severely influences the relative time-scales of various processes and it is not, at present, possible to simulate sufficiently realistic situations. A fluid approach, such as the MHD equations, does not handle particle effects. This can only be used to investigate macroscopic effects, and thus has to rely on a parametric description of particle processes like anomalous resistivity. Here we are only interested in examining what effect the anomalous resistivity has on the dynamics of turbulent current structures undergoing magnetic reconnection.

In this study, we discuss numerical experiments in which we choose the threshold velocity, $v_{\rm thr}$, to be $\xi$, $\sqrt{2}\,\xi$, and $\sqrt{3}\,\xi$, respectively. Note that $\xi$ is only a function of the electron temperature, $T_{\rm e}$, i.e., $\xi = \sqrt{2\,E_{\rm th}/m_{\rm e}} = \sqrt{k_{\rm B}\,T_{\rm e}/m_{\rm e}}$, and thus, $v_{\rm thr}$ depends on $T_{\rm e}$ as well. If we assign some critical value of energy corresponding to $v_{\rm thr}$, such as $m_{\rm e}\,v_{\rm thr}^2/2$, then the anomalous resistivity becomes active once this critical energy becomes equal to, or greater than $E_{\rm th}$, $2\,E_{\rm th}$, and $3\,E_{\rm th}$, respectively.

[1] This locally enhanced resistivity is anomalous resistivity in its own right too.

### 2.2. Basic equations

The full set of equations of dissipative MHD reads

$$\frac{\mathrm{D}\,\rho}{\mathrm{D}\,t} = -\rho\,\nabla\cdot\boldsymbol{U}, \tag{2}$$

$$\rho\,\frac{\mathrm{D}\,\mathbf{U}}{\mathrm{D}\,t} = -\nabla\,P + \boldsymbol{j}\times\boldsymbol{B} - \nabla\cdot\hat{\tau}, \tag{3}$$

$$\nabla\cdot\boldsymbol{B} = 0, \tag{4}$$

$$\frac{\mathrm{D}\,\boldsymbol{B}}{\mathrm{D}\,t} = \boldsymbol{B}\cdot\nabla\,\boldsymbol{U} - \boldsymbol{B}\,\nabla\cdot\boldsymbol{U} - \nabla\times\left[\left(\eta+\eta_{\mathrm{loc}}+\hat{\eta}\right)\nabla\times\boldsymbol{B}\right], \tag{5}$$

$$\frac{\mathrm{D}\,e}{\mathrm{D}\,t} = -\gamma\,e\,\nabla\cdot\boldsymbol{U} - \nabla\cdot\boldsymbol{q} - L_{\mathrm{r}} + S + Q_{\mathrm{visc}} + Q_{\mathrm{Joule}}. \tag{6}$$

Here $\mathrm{D}/\mathrm{D}t \equiv \partial/\partial t + \boldsymbol{U}\cdot\nabla$, and $\gamma$, $\rho$, $e$, $\boldsymbol{U}$, $\boldsymbol{B}$, $\boldsymbol{j}$, $\eta$, $\hat{\eta}$, $\hat{\tau}$, $Q_{\mathrm{visc}}$, $Q_{\mathrm{Joule}}$, $\boldsymbol{q}$, $S$, $L_{\mathrm{r}}$ are the adiabatic index, mass density, thermal energy, fluid velocity, magnetic field, electric current density, magnetic diffusion coefficient (numerical), coefficient of anomalous magnetic diffusion[2], viscous stress tensor (numerical), viscous dissipation, Joule dissipation, heat flux, volumetric heating rate, and radiative losses, respectively. Also, by $\eta_{\mathrm{loc}}$ we denote a coefficient of localized magnetic diffusion needed in our study to perturb the initial equilibrium plasma, and thus initiate a process of magnetic reconnection. The physical variables $\boldsymbol{j}$, $P$, $\boldsymbol{q}$, and $L_{\mathrm{r}}$, are given explicitly by

$$\boldsymbol{j} = \nabla\times\boldsymbol{B},\; P = e\,(\gamma-1) = \rho\,T, \tag{7}$$

$$\boldsymbol{q} = -\kappa_{\parallel}\,\nabla_{\parallel}\,T,\;\text{and}\;L_{\mathrm{r}} = n_{\mathrm{e}}\,n_{\mathrm{p}}\,Q(T). \tag{8}$$

Here $\kappa_{\parallel}$ is the field-aligned thermal conduction given through[3] $\kappa_{\parallel} = \kappa_0 T^{5/2}$, while $n_{\mathrm{e}}$ and $n_{\mathrm{p}}$ are the electron and proton number densities, respectively. For the radiative loss function, $Q(T)$, we choose the form given by Cook et al. (1989), calculated assuming photospheric abundance. Note also that we work in units where the universal gas constant equals the mean molecular weight.

### 2.3. Initial state

We consider the same model of a 2D magnetized atmosphere presented in Roussev et al. (2001). We allow for a shallow temperature gradient along the field lines, and thus examine physical circumstances that represent a solar transition region[4]. The effect of gravity is neglected for the sake of simplicity.

[2] We work in units where the magnetic permeability is set to 1, and thus the resistivity and magnetic diffusivity are the same transport coefficient from the numerical point of view.

[3] Subscript $\parallel$ refers to values along the magnetic field lines. The cross-field conduction is neglected, but could be important (e.g., Athay 1990) in lower transition region.

[4] This crude model has shallow temperature gradients and is more akin to the "cool loop" physical picture than the classical conductively heated models (see Mariska 1992, Sect. 7.6).

**Table 1.** Normalization units.

| Physical Quantity | Notation | Typical Value |
|---|---|---|
| Length | $L_0$ | $3\times10^8$ (cm) |
| Velocity | $V_{A0}$ | $1.293\times10^7$ (cm s$^{-1}$) |
| Time | $t_{A0}$ | 23.2 (s) |
| Density | $\rho_0$ | $5.02\times10^{-14}$ (g cm$^{-3}$) |
| Temperature | $T_0$ | $1\times10^5$ (K) |
| Magnetic field | $B_0$ | 8 (G) |

We refer to Roussev et al. (2001) for a detailed description of the initial configuration. Note that all the formulas and relations presented below are given in terms of normalized physical quantities and model parameters. The normalization units adopted in this study are given in Table 1.

In terms of normalized physical quantities and model parameters, the initial physical configuration reads

$$\boldsymbol{u} = 0, \tag{9}$$

$$b_x = 0,\; b_y = \tanh\left(\delta\,x^*\right), \tag{10}$$

$$e^* = \frac{1}{2(\gamma-1)}\left(1+\beta-b_y^2\right), \tag{11}$$

$$\rho^* = \left[\frac{\left(1+\beta-b_y^2\right)}{\beta}\right]^{\theta} \times\left\{1+\Delta\rho\left\{1-\tanh\left[\epsilon\left(y^*+y_{\mathrm{s}}^*\right)\right]\right\}\right\}, \tag{12}$$

and

$$T^* = (\gamma-1)\,\frac{e^*}{\rho^*}\cdot \tag{13}$$

Note that the $(x,y)-$plane is envisage as a vertical slice through the solar atmosphere. Here $\beta$ is the plasma "beta" parameter, $\delta$ is a model parameter used to control the width of the current concentration, $\epsilon$ controls the steepness of the transition region, $\theta$ is a free parameter (one over the polytropic index) which controls the density profile across the current concentration, and $\Delta\rho$ is a parameter which defines the density (and also temperature) jump across the transition region, i.e., $2\Delta\rho+1$, respectively. Assigned values for these parameters are summarized in Table 2.

The initial temperature is defined by Eqs. (11)–(13). Energy balance in the initial state requires the 2D spatial distribution of the volumetric heating sources to satisfy

$$S^* = \nabla^*\cdot\boldsymbol{q}^* + L_{\mathrm{r}}^*;\;\;\text{at}\;\;t^* = 0. \tag{14}$$

This way, the initial physical state is ensured to be in static equilibrium. During the whole computations, we maintain the volumetric heating rate, $S^*$, at its initial spatial values (Roussev et al. 2001).

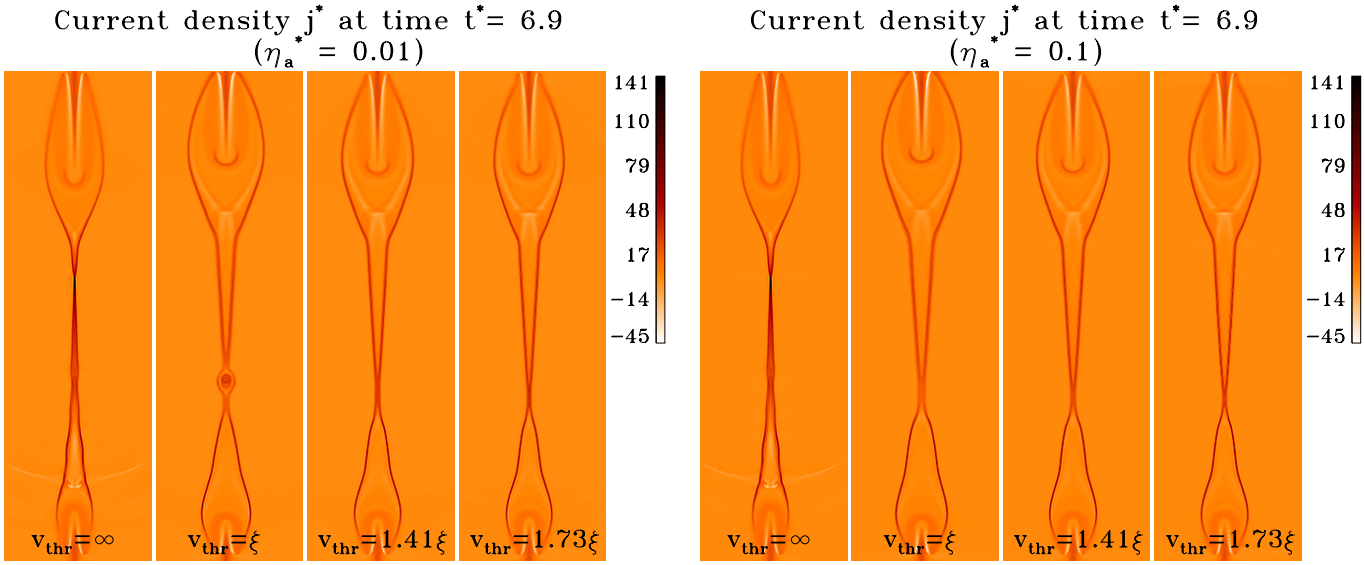


**Fig. 1.** Images of the $z-$component (component out of the plane of computational domain) of the current density, $j^*$, are shown in the case of $\eta_a^* = 0.01$ (left panel) and $\eta_a^* = 0.1$, respectively. The reference experiment "R" is shown to the far left on each panel, while the "A(B)" experiments appear from left to right as follows, A(B)1, A(B)2, and A(B)3, respectively. All images are shown at the same instant of time, $t^* = 6.9$. The dynamical range of the images is scaled with respect to the same minimum and maximum values of the current density, as derived for all of the experiments at this time. The gray-scale bar attached shows the translation table value versus degree of gray-scale. The threshold condition for the onset of anomalous resistivity is indicated at the bottom of each image.

**Table 2.** Listing of the common parameters and their assigned values.

| Parameter | Value | Parameter | Value |
|---|---|---|---|
| $\delta$ | 25 | $\beta$ | 0.164 |
| $\epsilon$ | 7 | $\alpha$ | 150 |
| $\Delta\rho$ | 4.5 | $\eta_0^*$ | 1/200 |
| $\theta$ | 0.3 | $t^*_{\rm rise}$ | 0.05 |
| $\gamma$ | 1.667 | $t^*_{\rm off}$ | 1 |
| $y^*_{\rm s}$ | 1.2 | $y^*_0$ | 1.2 |

### 2.4. Initial driver of magnetic reconnection

Similar to our previous related study (Roussev et al. 2001), magnetic reconnection is initiated in an ad hoc manner. This is achieved by letting a localized magnetic diffusion, $\eta^*_{\rm loc}$, begin to dissipate the 2D current sheet. This also forces the magnetic field to start reconnecting in a 2D $X$-point fashion. This localized diffusion is assigned for a finite time, and the explicit form of diffusivity is chosen as

$$\eta^*_{\rm loc}(x^*, y^*; t^*) = \eta^*_0 F^*(t^*) \times \exp\left\{-\alpha\left[x^{*2} + (y^* + y^*_0)^2\right]\right\}, \quad (15)$$

where

$$F^*(t^*) = \begin{cases} \frac{t^*}{t^*_{\rm rise}}; & 0 \le t^* \le t^*_{\rm rise}, \\ 1; & t^*_{\rm rise} < t^* \le t^*_{\rm off}, \\ 0; & t^*_{\rm off} < t^*. \end{cases} \quad (16)$$

Here $\eta^*_0$ is the normalized value of the localized magnetic diffusion coefficient, defined as reciprocal of some characteristic magnetic Reynolds number, $R_{\rm m} = 1/\eta^*_0$. The spatial shape of $\eta^*_{\rm loc}$ is chosen as a double Gaussian profile, with the $\alpha$ parameter determining the half width. The diffusion term given by Eq. (16), linearly increases from time $t^* = 0$ until $t^*_{\rm rise}$, followed by a constant value of diffusivity up to $t^* = t^*_{\rm off}$. At time $t^*_{\rm off}$, the dissipative term is switch off, and thus the system is let evolve by itself.

The position of the localized magnetic diffusivity patch along the current concentration is controlled by the parameter $y^*_0$. Assigned values for various driver parameters used in the present modeling are summarized in Table 2 (right column).

### 2.5. Set of experiments

The reconnection initiated through Eq. (16) leads to non-steady dynamics at $t^*_{\rm off} = 1$, and is then let evolve on its own. Once a critical state is encountered, the anomalous resistivity becomes active. We examined the subsequent dynamics of 2D magnetic reconnection for two normalized values of the anomalous resistivity, namely $\eta^*_a = 0.01$, and 0.1, respectively. We also performed an experiment where $\eta^*_a$ and $v_{\rm thr}$ were set to zero and infinity (experiment "R"), respectively. In this particular setup, the anomalous resistivity never turns on. The variety of experiments that are carried out is summarized in Table 3.

All numerical experiments are performed using a 2D compressible MHD code based on staggered meshes (for more details see Nordlund & Galsgaard 1995;

**Table 3.** Set of experiments.

| Reference Experiment ($\eta_a^* = 0$) | R | | |
|---|---|---|---|
| Threshold Velocity | $\xi$ | $\sqrt{2}\,\xi$ | $\sqrt{3}\,\xi$ |
| $\eta_a^* = 1/100$ | A1 | A2 | A3 |
| $\eta_a^* = 1/10$ | B1 | B2 | B3 |

Roussev et al. 2001). The MHD equations are solved in a 2D stretched grid, where stretching is applied only across the current concentration. This is done in order to resolve the region around the current concentration where the most important dynamics take place.

The 2D grid in which the seven experiments are carried out is of size $N_x \times N_y = 400 \times 700$. The numerical domain is chosen to be of size $[2\,x^*_{\rm max}, 2\,y^*_{\rm max}] = [6, 6]$. The stretching of the grid in the $x^*-$direction is applied in such a way that 50% of the grid points are allocated within $-0.7 \leq x^* \leq 0.7$. The smallest grid-spacing across the current concentration is assigned at $x^* = 0$, and corresponds to $(\Delta\,x^*)_{\rm min} = 6.05 \times 10^{-3}$. The grid-spacing at the $x^*-$boundaries is longer than this because of the stretching applied, and is equal to $(\Delta\,x^*)_{\rm max} = 7.05 \times 10^{-2}$. In contrast, the grid-spacing in the $y^*-$direction is uniform, and $\Delta\,y^* = 8.67 \times 10^{-3}$.

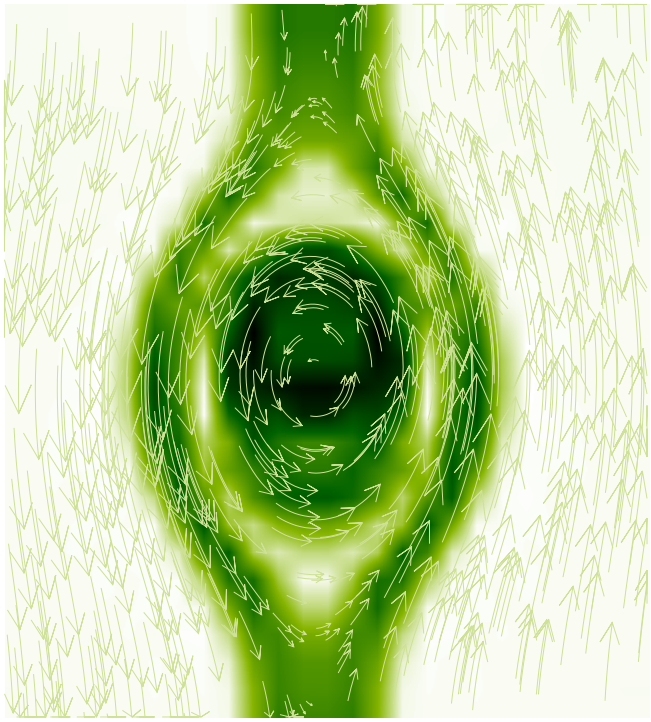

**Fig. 2.** Close-up of the $z-$component of the current density (shown as a background shading), and the magnetic field (short streak lines) at the region where the O-point is formed. These are shown at the same instant of time as in Fig. 1.

## 3. Discussion of numerical results

### 3.1. Dynamic consequences of the inclusion of anomalous resistivity

In all experiments presented above, the ad hoc localised magnetic diffusion is induced for a finite time. This forces the magnetic field involved in the diffusion region to start reconnecting. The magnetic diffusion is assigned for one time unit[5] ($t^*_{\rm off} = 1$), and is turned off before a steady state reconnection can be reached. In the following, we assess the role of anomalous resistivity on the dynamics of 2D magnetic reconnection for various normalised scaling values of this resistivity and threshold criteria for its onset.

#### 3.1.1. Case "R", $\eta^*_{\rm a} = 0$

The dynamics of magnetic reconnection in the reference experiment, "R", is similar to that discussed in Roussev et al. (2001), except that in the latter case, the localised magnetic diffusion operates for 5 time units, instead of 1 assigned here.

Once the localised magnetic diffusion is switched on, the initial pressure balance in the 2D current concentration is no longer maintained. As a dynamical consequence of this, the magnetic field begins to reconnect and plasma is pulled out from the diffusion region by the reconnected field lines. Both the kinetic gas and magnetic pressures decrease in the diffusion region, and thus an inflow of material towards the centre of this region is dynamically formed. This physical picture then evolves into the classical scheme of 2D $X$-point reconnection.

As reconnection proceeds, two reconnection jets are naturally formed, propagating in opposite directions along the initial current concentration. The thermal energy of the jets gradually increases in time, leading to dynamic expansion in the direction perpendicular to the magnetic field. Since this takes place between two low plasma "beta" regions, the increased pressure gradient across the magnetic field lines is easily balanced by magnetic tension forces outside the initial current structure. Thus, the jet expansion perpendicular to the current "sheet" is limited.

The border between the jets and the ambient field is located where the inflow of material becomes supersonic with respect to the slow MHD mode, and thus slow-mode shocks are dynamically formed. They can be traced by the locally enhanced value of the current density, $j^*$, as seen in Fig. 1. These shocks also reveal a distinct tulip-like shape of the reconnection driven jets.

Once the driver is switched off (at time $t^*_{\rm off} = 1$), the rate at which the electric current at the $X$-point dissipates decreases significantly. The stagnation flow initiated by the forced magnetic reconnection continues though. This results in an increase of the current density in the former diffusion region, as well as an increase in both the mass density and thermal energy there. The collapse continues

[5] In our notations this is one Alfvén travel time, $t_{A0}$.

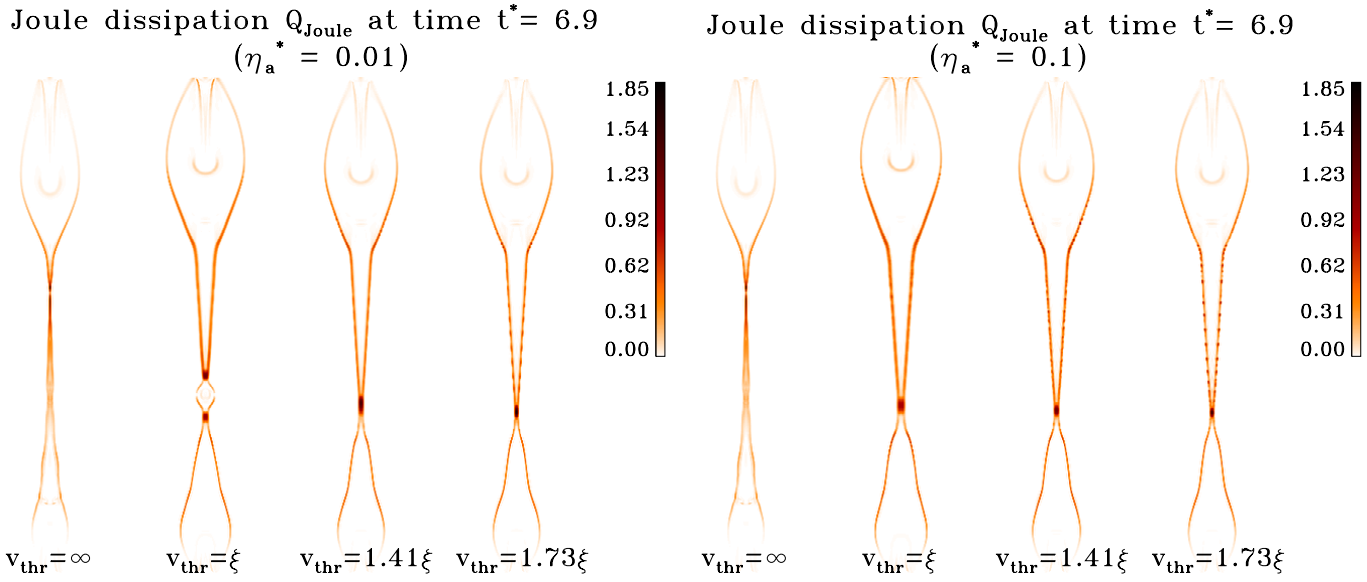


**Fig. 3.** Images of the Joule heating rate, $Q_{\rm Joule}$, for the case of $\eta_{\rm a}^* = 0.01$ (left panel) and $\eta_{\rm a}^* = 0.1$, respectively. The reference experiment "R" is again shown to the far left on each panel, while experiments "A(B)" appear from left to right in the same order as in Fig. 1. For better comparison, all images are scaled with respect to the same minimum and maximum values of Joule heat, as derived for all of the experiments.

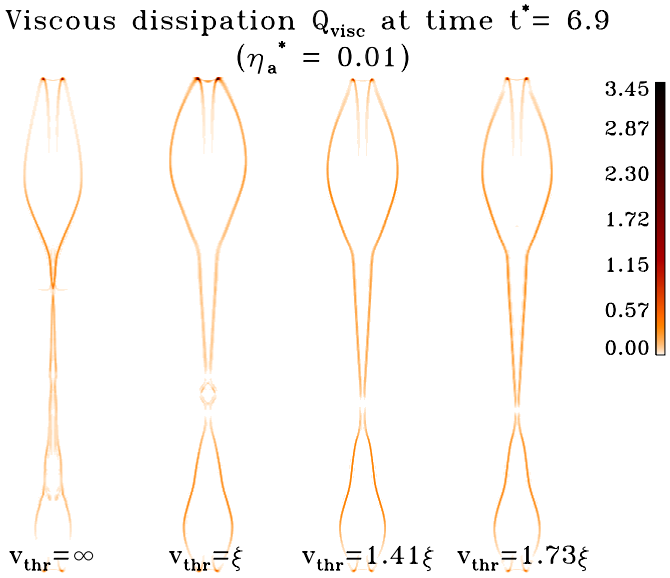


**Fig. 4.** Images of the viscous heating rate, $Q_{\rm visc}$, relevant to the case of $\eta_{\rm a}^* = 0.01$ are shown. The results for $\eta_{\rm a}^* = 0.1$ look similar. All images are scaled with respect to the same minimum and maximum values of viscous heat, as derived for all of the experiments shown.

to take place until a new balance is reached between the Lorentz force and the gas pressure gradient.

The position of maximum absolute value of the current density gradually moves along the jet symmetry axis ($x^* = 0$) in the positive $y^*-$direction (towards the high-temperature region of the initial background plasma; from bottom to top in the relevant image). This occurs as the current sheet gradually lengthens, which takes place because the current density never again reaches a magnitude at which the reconnection becomes important. As a result, the last reconnected field lines drag out the plasma trapped between the non-reconnected field lines, as it moves towards the heads of reconnection jets. A clear asymmetry between the two jets along $y^*$ is seen in this process. The jet propagating towards the dense plasma region, however, suffers much less from the stretching of the current sheet, because the plasma "beta" is higher here, which slows down the collapse.

The peak flow velocity inside the jet propagating towards the high-temperature region reaches the Alfvén speed, $V_{A0}$, of the outside region (see Table 1) at $t^* \approx 6$, followed by a very slight decrease onwards until the experiment is terminated. An investigation on the long-term behaviour of terminated magnetic reconnection is in progress; Galsgaard & Roussev (2001).

The analysis made so far applies to the reference case, "R", where the anomalous resistivity is never activated. All other experiments share the same dynamics until the point when the driver of magnetic reconnection is turned off.

### 3.1.2. Case of $\eta_{\rm a}^* = 0.01$

All "A" experiments refer to a normalised value of the anomalous resistivity chosen as $\eta_{\rm a}^* = 0.01$ (see Table 2). This corresponds to a characteristic magnetic Reynolds number of 100.

Once the ad hoc diffusion is turned off, the current density in the former magnetic diffusion region increases

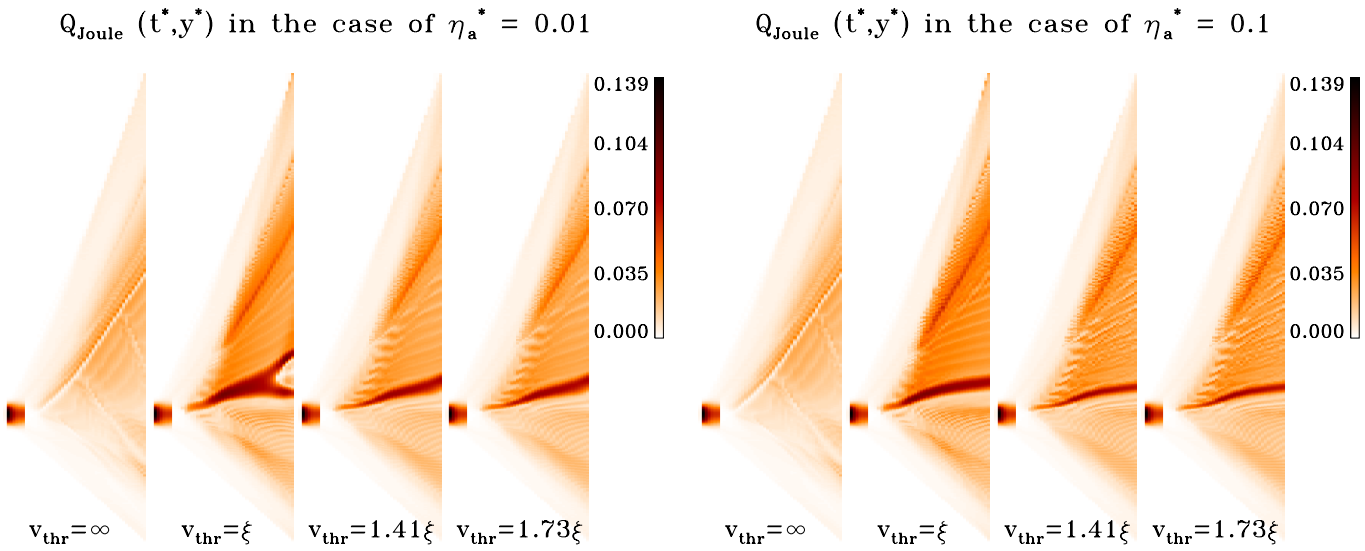


**Fig. 5.** Shown here are images of the averaged Joule heat across the initial current concentration over a spatial region of 2.4 arcsec (see text for more details). The left panel refers to the case of $\eta_a^* = 0.01$, while the right one represents the experiments with $\eta_a^* = 0.1$. Note that in each individual image time progresses from left to right. From bottom to top is shown the distribution of the averaged $Q_{\rm Joule}$ along the line-of-interest.

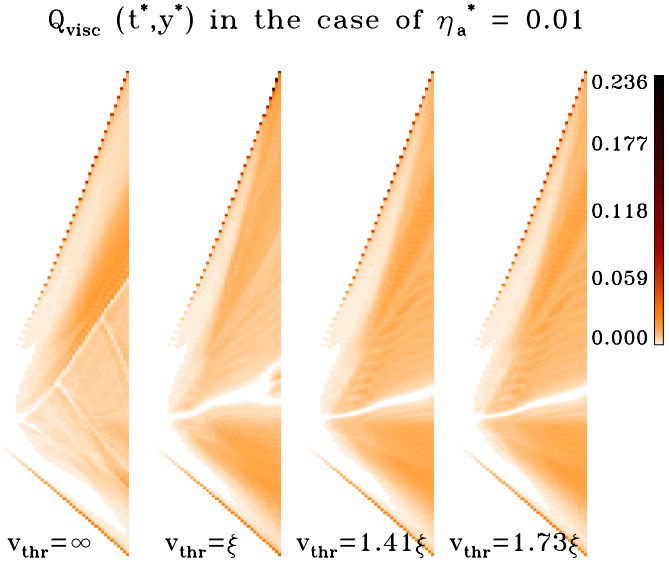


**Fig. 6.** Images of the averaged viscous heat over the same spatial region of 2.4 arcsec are shown. These are relevant to the case of $\eta_a^* = 0.01$. The results for $\eta_a^* = 0.1$ look similar.

on a short dynamic time-scale. The threshold condition for triggering anomalous resistivity is reached first in experiment "A1" at $t^* = 1.35$, and last in experiment "A3" at $t^* = 1.65$, as expected.

The current density for the four experiments, "R", "A1", "A2", and "A3", at the final time, $t^* = 6.9$, is shown in the left panel of Fig. 1. All images here are scaled with respect to the same dynamical range of the current density. The biggest differences are seen between experiments "R" and "A1". The reconnection jets in "A1" appear more extended perpendicular to the jet symmetry axis than those in "R". This is due to the fact that the fast onset of anomalous resistivity in the former ad hoc diffusion region in experiment "A1" leads to a further feeding of the two jets with newly reconnected field lines, preventing the diffusion region from the collapse encountered in experiment "R".

The anomalous resistivity first becomes active at the $X$-point, where the most rapid increase of the electric current takes place. As time progresses, the anomalous resistivity also activates along the standing slow-mode shocks. The consequent enhanced current dissipation there weakens the Lorentz forces, thus resulting in a slight increase of both jets opening angle and width of their heads.

An interesting feature is present in experiment "A1". A close-up of the magnetic field configuration reveals the presence of a magnetic island, or plasmoid. This structure is shown in Fig. 2. The background shading in this figure represents the current density, while the topology of the magnetic field is shown by plotting short field line traces.

The plasmoid shown in Fig. 2 is formed due to a pitchfork bifurcation (according to Priest et al. 1996) of the magnetic field line topology. This occurs as a consequence of the dynamic changes of the physical variables in the diffusion regions. In the particular setup of experiment "A1", the effect of anomalous resistivity at the $X$-point is to significantly increase the Joule dissipation. At one stage, the increase in plasma temperature occurs faster than that of the current density. This raises the plasma pressure, and thus slows down the plasma compression at the $X$-point region. As the thermal velocity of electrons raises the threshold value for the onset of anomalous resistivity faster than the current strength increases, the

anomalous resistivity locally switches off at the $X$-point. In the regions on either side of the $X$-point along the jet symmetry axis, the anomalous resistivity continues to operate. As a result, the ongoing magnetic reconnection in these regions form two new $X$-points. These feed the space between them with reconnected magnetic field, thus leading to the formation of a plasmoid.

The newly reconnected field lines originating from the two new $X$-points continuously add both magnetic flux and hot plasma into the plasmoid. Since the thermal conduction transports heat only along magnetic field lines, a rise in both temperature and thermal energy at the O-point is inevitable. As a dynamic reaction to the increase in both the magnetic and kinetic gas pressures, the plasmoid gradually expands. Because of the increased gas pressure, the two $X$-points are pushed further apart. Current dissipation due to the anomalous resistivity continues to take place in the separator shell surrounding the plasmoid. As a result, the Lorentz force supporting the separator shell weakens even more, thus helping its further expansion.

In turn, such a physical situation is not encountered in experiments "A2" and "A3". This is due to the fact that the rate of Joule dissipation produced by the anomalous resistivity never becomes high enough for the threshold condition to break down, and thus locally turn off the dissipation process.

By comparing experiments "A1" through "A3", the effect of different threshold drift velocities can be assessed. A low threshold allows the diffusion to become active earlier than at a higher value. This is why the current in the low threshold experiment, "A1", is more diffused and has lower values compared to that in the high threshold experiment, "A3".

#### 3.1.3. Case of $\eta_a^* = 0.1$

All of the "B" experiments refer to the case where the normalised value of anomalous resistivity is set to 0.1 (characteristic magnetic Reynolds number of 10). Relevant images of the current density appear in the right panel of Fig. 1, shown at the same current time, as well as scaled in the same dynamical range.

The main difference between the case of $\eta_a^* = 0.1$ and that of $\eta_a^* = 0.01$ appears, as expected, in the rate of electric current dissipation. The higher the normalised value of anomalous resistivity is, the higher the value of the associated Joule dissipation. As to the importance of $v_{thr}$, the lower the threshold drift velocity, the sooner the anomalous resistivity becomes activated. As a result of this, more Joule heat is released. The same conclusion was drawn in the previous analysis of the "A" experiments.

In the "B" experiments, it is found that the anomalous resistivity operates in an "on-off" manner. The dissipation of electric current is so fast here, that soon after this process is activated, it switches off again. The higher the value of $\eta_a^*$, the faster the dissipation of electric current and the more frequently the process of anomalous resistivity switches on and off.

Despite the fact that the dissipation of electric current happens faster in experiments "B" than in experiments "A", there is no formation of a magnetic island in the former. This is because the anomalous resistivity repeatedly turns on and off here. Such circumstances prevent the Joule dissipation from rapidly increasing the plasma temperature enough to switch off the anomalous resistivity for long enough to form a plasmoid.

### 3.2. Joule and viscous dissipations

It is of interest in the present study to analyse the temporal and spatial behaviour of the Joule and viscous dissipations for the two normalised values of anomalous resistivity and for various threshold conditions.

#### 3.2.1. Spatial distribution of the dissipation at $t^* = 6.9$

The Joule heating rate, $Q_{Joule}$, at $t^* = 6.9$ is shown in Fig. 3, while Fig. 4 presents the rate of viscous dissipation, $Q_{visc}$, at this time. The left panel in Fig. 3 refers to the case of $\eta_a^* = 0.01$, while the right one shows results from the experiments with $\eta_a^* = 0.1$. As for the viscous dissipation, we show only results obtained for the "A" experiments, since the differences between experiments "A" and "B" are insignificant. All images are scaled with respect to the maximum and minimum values of $Q_{Joule}$ (in Fig. 3), and $Q_{visc}$ (in Fig. 4), respectively, as derived for all experiments presented here.

In the reference experiment, "R", the magnetic dissipation is caused by a numerical resistivity designed to prevent the code from generating unresolved current concentrations under various physical conditions (for a full description of the relevant numerical algorithm see Nordlund & Galsgaard 1995). In order to minimise the current dissipation throughout the computational domain, the (explicit) numerical algorithm combines a zero and second difference dependence of the current density on the spatial coordinates, together with a discontinuities capturing scheme applied in regions of strong magnetic compression. In the present model, the numerical resistivity dissipates the current at the locations of slow-mode shocks and at the bow shocks formed in front of the reconnection driven jets. In experiments "A" and "B", however, the dissipation is dominated by the anomalous resistivity, with the bulk Joule dissipation taking place at the slow MHD shocks.

By comparing the three "A(B)" experiments shown in Fig. 3, one can infer that at low values of the threshold drift velocity, the anomalous resistivity takes place over an increasing fraction of the surface wrapping the standing slow-mode shocks. This preferably happens towards the high-temperature region of the initial background plasma. Furthermore, the Joule dissipation at the bow shocks due to the anomalous resistivity is stronger at small $v_{thr}$, rather than at high values of this critical drift

velocity. Notice also the dark spots of strong current dissipation along the slow-mode shocks visible in the images of experiments "A3" and "B3". As already inferred above, this is due to the "bursty" manner the process of anomalous resistivity operates at a high value of the threshold criterion.

In experiment "A1", Fig. 3 shows that strong current dissipation takes place at the two $X$-points. These feed magnetic flux into the growing plasmoid formed between them. Current dissipation, though weaker than at the $X$-points, is also found along the separator lines defining the boundary between the plasmoid and surrounding magnetic field.

Phenomenologically, the background viscosity is split into two parts – shear and bulk viscosity. The shear contribution is defined by the absolute values of the first and third cross differences of the fluid velocity. The bulk viscosity, in turn, depends linearly on the absolute value of the convergence of the velocity field, and is zero where the divergence of this field is positive. The bulk viscosity therefore operates at the locations of strong shocks (for details refer to Nordlund & Galsgaard 1995).

Figure 4 only shows the viscous dissipation in the "A" experiments, since the dissipation in the "B" experiments looks very similar. All images are again scaled with respect to the same maximum and minimum values of $Q_{\rm visc}$, as derived for all of the experiments shown. In this figure, one can see that most of the viscous dissipation coincides with the bow shocks formed in front of each reconnection jet, and that it is also present at the locations of slow-mode shocks.

### 3.2.2. Average dissipation rates as functions of time

Figures 5 and 6 show the averaged Joule and viscous dissipation, respectively, across the entire jet structure as a function of time. For this purpose, we choose as a line-of-interest the jet symmetry axis, and then average both $Q_{\rm Joule}$ and $Q_{\rm visc}$ over the maximum spatial extend of the reconnection jets along $x^*$, as derived for all of the experiments. This maximum spatial extent is reached in experiment "A1" and in physical units corresponds to 1745 km, i.e., ≈2.4 arcsec on the surface of the Sun. Results for the $\eta_{\rm a}^* = 0.01$ case are shown in the left panel of Fig. 5, while the right one refers to the case of $\eta_{\rm a}^* = 0.1$. Note that time progresses from left to right, while the $y^*-$coordinate increases from bottom to top. The limited quality of the images is due to the finite time resolution of the saved MHD data[6]. The scaling of the images is done with respect to the same maximum value of the averaged $Q_{\rm Joule}$ in all of the experiments.

The region of the initial driver is easily recognized in this figure as a short-lived dark feature at the left edge of all sub-images. This is where most of the Joule dissipation is released until the ad hoc diffusivity is turned off at time $t = t_{\rm off}^*$. Following the disappearance of the ad hoc diffusivity, one can see both the time-delay before the anomalous resistivity first becomes active, and its preferred location in each experiment. The dark regions of strong Joule dissipation first appear where the peak current is reached along the jet symmetry axis, and later at the locations of the slow-mode shocks. It is also seen in Fig. 5 that, as time progresses, the location of strong Joule dissipation moves towards the hot plasma regions (from bottom to top). Notice also how these dark regions become thinner as $v_{\rm thr}$ is increased, especially in the images of experiments "B" (right panel). This is due to the fact that the anomalous resistivity is induced in less spatial locations as the threshold drift velocity is increased.

The second image in the left panel of Fig. 5 reveals the bifurcation of the diffusion point and the subsequent formation of the plasmoid. The two $X$-points feeding the plasmoid are recognized as two dark regions of strong current dissipation.

Figure 6 shows the averaged $Q_{\rm visc}$ as a function of time (from left to right), and position along the line-of-interest (from bottom to top) for experiments "A" Corresponding results for the "B" experiments look similar. Here it is seen that the averaged viscous dissipation predominantly occurs at the bow shocks formed in front of the reconnection jets. By comparing Figs. 5 and 6, one can see clear differences in the spatial locations where the viscous and Joule dissipations take place. There is hardly any viscous dissipation seen in the regions where the anomalous resistivity is active. This implies that the plasma heating due to the two processes occurs at very different physical locations along the reconnection jets.

### 3.2.3. Total energy output

It is of general interest to estimate the energy output, in physical units, during the reconnection events examined here. For this purpose, we computed the total energy release, $E_{\rm tot}$, in a vertically oriented slab (cylinder) which contains the maximum spatial extend of the reconnection jets reached at time $t^* = 6.9$. The vertical length of this slab is $6\,L_0 = 18\,000$ km (refer to Table 1) and its diameter is 1745 km. Scaled to the Sun, the latter corresponds to ≈2.4 arcsec.

The total energy release, $E_{\rm tot}$, is defined as the sum of the integrated Joule, $E_{\rm Joule}$, and viscous, $E_{\rm visc}$, dissipation over the whole volume of this slab and physical time. Corresponding values are computed in CGS units and $E_{\rm tot}$ is derived as a function of time. Values of $E_{\rm Joule}$, $E_{\rm visc}$, and $E_{\rm tot}$, obtained at the end of all of the experiments are given in Table 4. For better comparison, the total Joule dissipation at the end of each experiment is also given relative to the value of the reference experiment, "R". These values are given in the parentheses. On average, the total Joule dissipation in all "A" and "B" experiments is 1.71 times larger than that in the reference experiment.

[6] Note here that snapshots in all experiments are taken every $\Delta\, t^* = 0.15$.

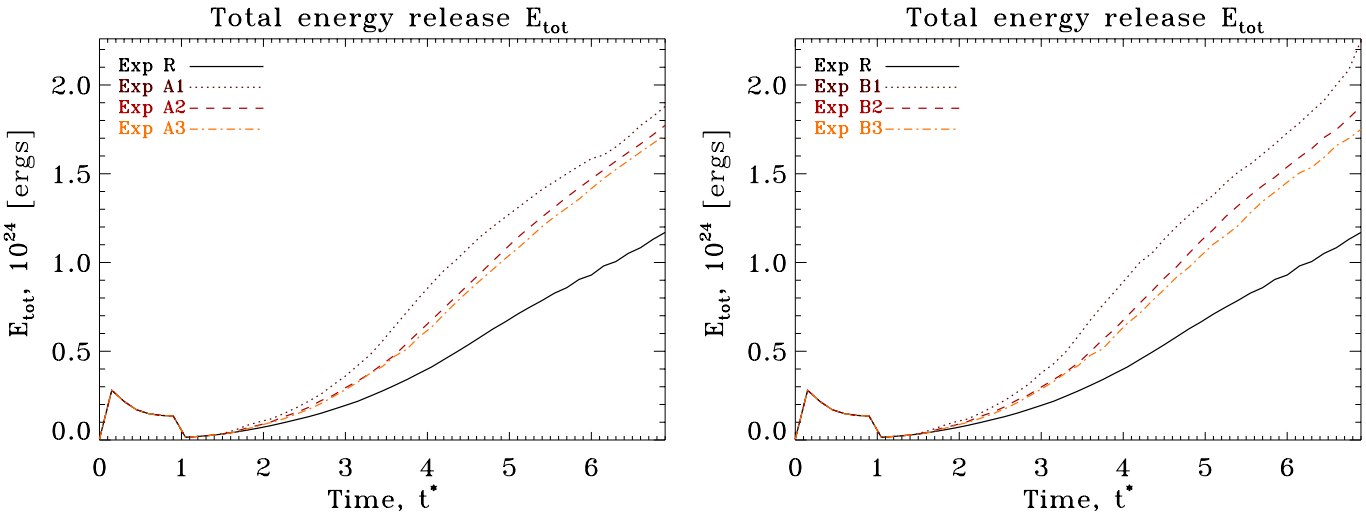


**Fig. 7.** The total energy release, $E_{\rm tot}$, is shown as a function of time for the reference, "R", and all "A" experiments (left panel), as well as all of the "B" experiments, respectively. For better comparison, both panels are scaled with respect to the same maximum value of energy release (see text for more details).

Figure 7 shows $E_{\rm tot}$ as a function of time. Corresponding results for the reference "R" and all "A" experiments are shown in the left panel of Fig. 7, while the right one refers to all of the "B" experiments. For better comparison, $E_{\rm tot}$ is scaled with respect to the same maximum value of $2.26 \times 10^{24}$ ergs.

As seen in Fig. 7, the largest energy release occurs for a small threshold drift velocity, i.e., in the particular setup of experiments "A1" and "B1". This is to be expected, since in these cases the anomalous resistivity first becomes active, as well as dissipates the electric current at more spatial locations. Furthermore, the higher the normalized value of anomalous resistivity is, the larger the rate of current dissipation, and therefore the larger the total amount of released Joule heat. The "bursty" nature (see Sect. 3.1.3) is not seen here because of the spatial averaging.

**Table 4.** Summary on the energy output in the various experiments.

| Ref. Experiment | R | | |
|---|---|---|---|
| $E_{\rm Joule}$, $10^{24}$ ergs | 0.711 (1)[a] | | |
| $E_{\rm visc}$, $10^{24}$ ergs | 0.458 | | |
| $E_{\rm tot}$, $10^{24}$ ergs | 1.169 | | |
| Experiment | A1 | A2 | A3 |
| $E_{\rm Joule}$, $10^{24}$ ergs | 1.289 (1.81) | 1.154 (1.62) | 1.036 (1.46) |
| $E_{\rm visc}$, $10^{24}$ ergs | 0.589 | 0.618 | 0.682 |
| $E_{\rm tot}$, $10^{24}$ ergs | 1.878 | 1.772 | 1.718 |
| Experiment | B1 | B2 | B3 |
| $E_{\rm Joule}$, $10^{24}$ ergs | 1.557 (2.19) | 1.216 (1.71) | 1.049 (1.48) |
| $E_{\rm visc}$, $10^{24}$ ergs | 0.693 | 0.663 | 0.700 |
| $E_{\rm tot}$, $10^{24}$ ergs | 2.250 | 1.879 | 1.749 |

[a] These are normalized relative to case "R".

## 4. Summary

We examined the impact of anomalous resistivity on the dynamics of 2D magnetic reconnection. The initial physical conditions were considered to represent a "quiet" Sun transition region environment. The model situation involved a 2D unstratified atmosphere, where we allowed for a shallow temperature gradient along the field lines to simulate a transition region. This is a rather crude approach, unless a "cool loop" situation is present.

In the initial physical conditions, magnetic reconnection is initiated once an ad hoc localized magnetic diffusion starts to be induced in the 2D current structure formed between the two magnetic fluxes of opposite polarity. At a certain time after the driver of magnetic reconnection is turned off, some critical state in the current "sheet" is reached, leading to the inclusion of anomalous resistivity. This is assumed to be driven by a streaming instability, which occurs when the drift velocity of electrons exceeds their mean thermal speed. Such a process leads to the excitation of electron plasma waves (Langmuir plasma oscillations), and reduces the effective collision time of electrons down to $2\,\pi/\omega_{\rm pe}$, where $\omega_{\rm pe}$ is the electron plasma frequency. Thus, the resistive diffusion coefficient, $\eta$, is enhanced accordingly and becomes $\eta \cong c^2/2\,\pi\,\omega_{\rm pe}$ (Parker 1994).

In this study, it was assumed that the ion (at temperature $T_{\rm i}$) and electron (at temperature $T_{\rm e}$) fluids are in thermal equilibrium, and thus $T_{\rm e} \cong T_{\rm i}$. Once the above process starts taking place and anomalous resistivity arises, the electron fluid is preferably heated, making $T_{\rm e} > T_{\rm i}$. We then supposed there is an efficient collisional

coupling between the electrons and ions[7], making again $T_\mathrm{i}$ approach $T_\mathrm{e}$. If in reality this turns out not to be the case, then $T_\mathrm{e}$ will continue rising, thus leading to $T_\mathrm{e} \gg T_\mathrm{i}$. In such a situation, the one fluid approach is no longer valid, and therefore the electrons and ions must be treated as two separate fluids. Under such conditions of $T_\mathrm{e} \gg T_\mathrm{i}$, the criterion for developing ion-acoustic turbulence is momentarily fulfilled, since the latter is no longer subject to ion Landau damping. The anomalous resistivity produced by such turbulence is, however, by a factor of $\sqrt{m_\mathrm{e}/M_\mathrm{i}}$ times weaker than the above discussed in the case of $T_\mathrm{e} \cong T_\mathrm{i}$ (here $m_\mathrm{e}$ is the mass of electrons and $M_\mathrm{i}$ is the mass of ions, respectively). An investigation of this process was beyond the scope and intend of this study.

The onset of anomalous resistivity under the above condition of $T_\mathrm{e} \cong T_\mathrm{i} = T$ first occurs in the former diffusion region, where the current density starts rising right after the ad hoc diffusion is turned off. We explored various situations and examined the impact of both the threshold drift velocity and normalized value of anomalous resistivity on the dynamics of 2D magnetic reconnection.

It was found that, the lower the threshold velocity is, the earlier the anomalous resistivity becomes active and the larger the spatial regions effected by this diffusion. Furthermore, the lower the threshold velocity, the larger the amount of total Joule dissipation. At some high enough threshold and normalized value of the anomalous resistivity, the current dissipation occurs in a rapid switch "on-off" manner, leading to a "bursty" release of Joule heat. The higher the threshold values are, the less time the process of anomalous resistivity is active.

At low threshold and at some small enough normalized value of the anomalous resistivity, a rather interesting physical situation is encountered. As a result of local switch-off of the anomalous resistivity, a bifurcation of the magnetic field topology occurs, leading to the formation of a magnetic plasmoid.

On average, the total Joule dissipation in all experiments with anomalous resistivity being active is approximately twice that found in the "R" experiment involving only numerical diffusion. When the total energy release at the end of the experiments (at physical time $t = 160$ s) was converted into physical units, we obtained values that are above the lower limit of "quiet" Sun nano-flares required to maintain a hot corona (e.g., Parker 1988). In terms of dynamics, similar reconnection events were examined in our previous study (see Roussev et al. 2001). Those were found to appear as "velocity" events in the emission line profiles, which when applied to the case of the "quiet" Sun, could be addressed to solar explosive events.

Lastly, we note that a recent study by Winebarger et al. (1999) based on SUMER observations suggests that the energy flux provided by the numerous solar explosive events is comparable to that required to maintain a hot corona. These events are thus believed to have a strong impact on the energy balance of both the solar transition region and overlying corona.

[7] For $T = 10^5$ K and electron number density $n_\mathrm{e} = 3 \times 10^{10}$ cm$^{-3}$, the electron-ion collision time is of the order of $10^{-2}$ s.

*Acknowledgements.* The National Center for Atmospheric Research (NCAR) is sponsored by the National Science Foundation. Research at Armagh Observatory is grant-aided by the N. Ireland Dept. of Culture, Arts and Leisure, while partial support for software and hardware is provided by the STARLINK Project, which is funded by the UK PPARC. I. Roussev dedicates his studies to Ana and Elena. He is also thankful to the Department of Applied Mathematics, University of St. Andrews, and the NSO in Tucson, Arizona, for the support provided during his visits there. K. Galsgaard was supported by PPARC in the form of an Advanced Fellowship. The MHD experiments were carried out on the PPARC funded Compaq MHD Cluster in St. Andrews. We are all very thankful to Tom Holzer, Egil Leer, J. G. Doyle, and B. V. Somov for the useful comments and suggestions made while this manuscript was prepared.

## References

Athay, R. G. 1990, ApJ, 362, 364
Buneman, O. 1958, Phys. Rev. Lett., 1, 8
Cook, J. W., Cheng, C.-C., Jacobs, V. L., & Antiochos, S. K. 1989, ApJ, 338, 1176
Fried, B. D., & Gould, R. W. 1961, Phys. Fluids, 4, 139
Galsgaard, K., & Roussev, I. 2001, A&A, in preparation
de Kluiver, H., Perepelkin, N. F., & Hirose, A. 1991, Phys. Rep., 199 (6), 281
Lazarian, A., & Vishniac, E. 2000, in Astrophysical Plasmas: Codes, Models, and Observations, ed. J. Arthur, N. Brickhouse, & J. Franco, Rev. Mex. Astron. Astrofís. Conf. Ser., 9, 55
Low, B. C. 1994, Phys. Plasmas, 1, 1684
Magara, T., Mineshige, S., Yokoyama, T., & Shibata, K. 1996, ApJ, 466, 1054
Magara, T., Shibata, K., & Yokoyama, T. 1997, ApJ, 487, 437
Mariska, J. T. 1992, The Solar Transition Region (Cambridge University Press, Cambridge)
Nishikawa, K.-I., & Neubert, T. 1996, Adv. Space Res., 18, 263
Nordlund, Å., & Galsgaard, K. 1995 (private communication, `www.astro.ku.dk/~klaus/`), A 3D MHD Code for Parallel Computers
Parker, E. N. 1988, ApJ, 330, 474
Parker, E. N. 1994, Spontaneous Current Sheets in Magnetic Fields with Application to Stellar X-Rays, International Series on Astronomy and Astrophysics (Oxford University Press, Oxford)
Priest, E. R., Lonie, D. P., & Titov, V. S. 1996, J. Plasma Phys., 56, 507
Roussev, I., Galsgaard, K., Erdélyi, R., & Doyle, J. G. 2001, A&A, 370, 298
Silberstein, M., & Otani, N. F. 1994, J. Geophys. Res., 99, 6351
Spitzer, L. 1962, Physics of Fully Ionized Gases (Interscience, New York)
Somov, B. V., & Oreshina, A. V. 2000, A&A, 354, 703
Winebarger, A. R., Emslie, A. G., Mariska, J. T., & Warren, H. P. 1999, ApJ, 526, 471